Photocatalytic oxidative desulfurization and degradation of organic pollutants under visible light using TiO_2 nanoparticles modified with iron and sulphate ions

Josefa Ortiz-Bustos[a], Isabel del Hierro[a]*, Yolanda Pérez[a,b]*

[a] Departamento de Biología y Geología, Física y Química Inorgánica, Escuela Superior de Ciencias Experimentales y Tecnología, Universidad Rey Juan Carlos, C/ Tulipán s/n, 28933 Móstoles (Madrid), Spain.

[b] Advanced Porous Materials Unit, IMDEA Energy, Av. Ramón de la Sagra 3, 28935 Móstoles, Madrid, Spain

E-mail: yolanda.cortes@urjc.es

Abstract

The incorporation of iron and sulphate ions on TiO_2 nanoparticles has been carried out in order to enhance catalytic performance in environmental remediation. The aim of this work is to design a multifunctional and visible-light active photocatalyst to remove pollutants from transportation fuels and water. The influence of doping with sulphur and iron on the physical, structural, optical, and electrochemical properties of TiO_2 has been fully analysed by a wide variety of techniques. Thus, the incorporation of a low amount of iron improves the photocatalytic performance, as in the case of 1.2%S-0.5%Fe-TiO_2 photocatalyst, which shows the highest activity under visible light irradiation. The enhanced behaviour of the electron charge transfer of this photocatalyst has been confirmed by electrochemistry measurements including linear sweep voltammetry and electrochemical impedance spectroscopy. Also, the stability and recyclability of the best photocatalyst have been assessed.

Keywords: Titanium dioxide, photocatalytic oxidative Desulfurization, photodegradation, dibenzothiophene, ciprofloxacin.

1. Introduction

The development of efficient and sustainable technologies for the reduction of pollutant gas emissions (CO_2, NO_x, SO_x) and water pollution is one of today's greatest challenges. The combustion of sulphur-containing compounds in fuel oils produces noxious sulphur oxides (SO_x) which are directly released into the atmosphere. Thus, the reduction of sulphur content in fuels is urgently needed in order to avoid serious health and environmental problems caused by toxic gas emissions [1] and also to comply with strict regulations enforced for limiting sulphur content in liquid fuels [2]. In recent years, conventional hydrodesulfurization (HDS) technology has been employed for sulphur removal in transportation fuels; however, it requires high hydrogen pressure and elevated temperatures, which provoke an increase in the operating costs and loss of octane number [3]. Hence, photooxidative desulfurization has emerged as a promising alternative to the hydrodesulfurization process. TiO_2-based materials have been proved to be efficient photocatalysts for the removal of different sulphur compounds from fuels by desulfurization process [1]. Also, other systems based on composites have exhibited excellent visible photocatalytic activity, including Ti_3C_2/g-C_3N_4 [4], ATP-CeO_2/MoS_2 [5], CeO_2/ATP/g-C_3N_4 [6], MoO_3-MOF [7] and $BiP_{1-x}V_xO_4$/ATP [8].

On the other hand, emerging contaminants (including pharmaceutical, pesticides and personal care products) have frequently been found in wastewater treatment plants, even in freshwater, due to the fact that conventional treatments are ineffective for their complete elimination [9]. Specifically, the presence of antibiotics in wastewater is producing undesirable human and environmental concerns such as antibiotic-resistant bacteria and contamination of the aquatic environment [10]. In particular, fluorine-containing antibiotics (e.g. ciprofloxacin) are highly resistant to degradation and have been detected in higher concentrations than those of other drugs [11].

To solve these challenges, efficient removal technologies are being developed to avoid the environmental effects of pollutants. Among all of these, photocatalysis has currently emerged as an effective, sustainable, and economic technology to reduce the environmental pollution. In this regard, titanium dioxide is one of the most promising and cost-effective photocatalysts for the environmental pollutants removal as it can be easily modified to enhance its photocatalytic properties under visible light irradiation.

One of the approaches that has proven to be promising in this enhancement is cation and anion doping of TiO_2 due to the decrease in the band gap width and the suppression of electron-hole recombination [12]. To date, there are only a few studies that focus on TiO_2 materials modified with iron and sulphur for photocatalytic experiments. For example, Niu et al. [13] synthesized iron and sulphur co-doped TiO_2 photocatalysts by solvothermal method with $FeCl_3$ and potassium persulfate as iron and sulphur sources, respectively. They found that TiO_2 material with a ratio of Fe/Ti = 1.0 % exhibited the highest activity in phenol degradation. Co-doped S/Fe-TiO_2 materials synthesized by Christoforidis et al. [14] achieved a high selectivity in the photodegradation of toluene which was attributed to the influence of sulphur on the properties of the TiO_2 surface. These materials were prepared by microemulsion synthetic method using ammonium sulphate and iron (III) nitrate as S and Fe sources, respectively. Microflow system was employed by He et al. [15] to obtain active Fe-S-TiO_2 catalysts for the degradation of methyl orange using UV and visible light. More recently, Villaluz et al. have reported a new approach to prepare Fe/N/S-TiO_2 materials using ammonium iron (II) sulphate for removal of 4-chlorophenol [16]. To the best of our knowledge, there are no studies in the literature using iron and sulphate modified TiO_2 nanomaterials for both photocatalytic removal of sulphur-containing pollutant and an antibiotic drug.

Herein, TiO_2 nanoparticles have been modified with iron, a highly abundant and sustainable metal, and sulphate ions by using $Fe(NO_3)_3$ and Na_2SO_4 as chemical sources, respectively. The as-synthesized materials have been completely characterized and tested as versatile photocatalysts in the elimination of dibenzothiophene, as well as, in the degradation of ciprofloxacin with visible light irradiation. The latter is a highly stable drug that has been studied by electrochemical methods under visible light in the presence of iron and sulphate modified TiO_2.

2. Experimental Section

2.1. Materials

Titanium (IV) isopropoxide (TIPT), nitric acid 65 %, ciprofloxacin (> 98 %), dibenzothiophene were purchased from Sigma Aldrich-Merck. Iron(III) nitrate—water (1/9) ($Fe(NO_3)_3 \cdot 9H_2O$), sodium sulphate (Na_2SO_4) and hydrogen peroxide solution (H_2O_2) 30 % were purchased from Scharlab. Dodecane ≥ 99.8 % was acquired from Alfa Aesar,

2-propanol from VWR Chemicals and n-octane from Fluorochem. Water was obtained from a Millipore Milli-Q system (Waters, USA).

2.2. Synthesis of catalysts

2.2.1. Synthesis of TiO_2 nanoparticles modified with Fe^{3+} and SO_4^{2-} ions

The synthesis procedure of modified TiO_2 nanoparticles follows a typical sol-gel method, in which 40 mL of titanium (IV) isopropoxide were dissolved in 60 mL of 2-propanol and added dropwise to an aqueous solution of HNO_3 at pH = 2. $Fe(NO_3)_3 \cdot 9H_2O$ and Na_2SO_4 were used as the source of Fe^{3+} and SO_4^{2-}, respectively, and added dropwise at the same time to the acidic solution in different quantities (0.5-1 % for Fe and 0.6-1.5 % for S) previously dissolved in 100 mL of milliQ water. The pale orange mixture was vigorously stirred for 16 hours. Then, the suspension was filtered, washed and dried. Finally, the samples were calcined in air in an oven at 400 ^oC for 16 hours (0.8 ^oC/min) and labelled as X%Fe-TiO_2, Y%S-TiO_2 and Y%S-X%Fe-TiO_2, where X and Y are the real percentages of Fe and S incorporated in each sample, respectively.

2.3. Characterization

All the synthesized nanoparticles were characterized using the following techniques: X-Ray diffraction (XRD) patterns were carried out with a Phillips Diffractometer model PW3040/00 X'Pert MPD/MRD at 45 KV, 40 mA with Cu-Kα radiation (λ=1.5418 Å), adsorption-desorption isotherms of nitrogen and pore size distributions were obtained using a Micromeritics TriStar 3000 analyser applying the Barret- Joyner-Halenda (BJH) model, FTIR spectra were recorded on a Varian Excalibur Series 3100 – UMA 600 spectrometer in Attenuated Total Reflectance (ATR) mode. DRUV-Vis spectra (in diffuse reflectance mode) were obtained using a Varian Cary 500 spectrophotometer. The band gap values were obtained applying the Kubelka-Munk function [$F(R_\infty)$] to DRUV-Vis spectra. Thermogravimetric analysis was obtained under air atmosphere with a Star System Mettler Thermobalance in the range of 40 to 1000 ºC of temperature. Transmission electron microscope (TEM) studies were performed using a 2100 JEM (JEOL) electron microscope operating at 200 kV and Scanning Electron Microscope in high resolution (SEM-FEG) using a Nova NanoSEM 230 microscope. Fe content was determined by induced coupled plasma atomic emission spectroscopy (ICP-AES) using a 7300DV optical emission spectrometer from Perkin Elmer and S content was calculated

by elemental analysis on a CHNOS model Vario EL III of Elemental Analyses System. The electrochemical measurements were recorded with a potentiostat/galvanostat Autolab PGSTAT302 through modified carbon paste electrodes (MCPE) used as working electrode with the same procedure than in previous works [17]. Electrochemical impedance spectroscopy (EIS) data were recorded by using a potentiostat/galvanostat with an impedance module with AC signal of 10 mV amplitude in the frequency range between 0.01 Hz and 100 kHz in potentiostatic conditions. The electrode potentials were measured against a saturated Ag/AgCl(s) reference electrode. Some of the electrochemical measurements were performed in phosphate buffer at pH 7.4 or 0.2 M Na_2SO_4 solution using deionized water.

2.4. Photocatalytic Desulfurization of dibenzothiophene.

In this experiment, 20 mg of photocatalyst, 10 mL of n-octane (model oil) containing dibenzothiophene (100 ppm S), 10 mL of acetonitrile and hydrogen peroxide 30 % in different proportions were mixed in a 20 mL flask tube and stirred at room temperature under the irradiation of visible light produced via a 300 W Xenon lamp. After certain time, the reaction mixture was centrifuged, and the supernatant was analyzed by GC-FID (Perkin-Elmer GC Clarus 580) with a Velocity® column (dimethylpolysiloxane, 30 m, 0.25 mm, 1.00 µm) using dodecane as an external standard. The DBT conversion was calculated according to equation: Conversion (%) = [(initial mmoles of DBT - final mmoles of DBT)/initial mmoles of DBT] × 100.

2.5. Photocatalytic degradation of ciprofloxacin (CIP).

To perform the degradation reaction, the photocatalyst (8 mg) was suspended in an aqueous CIP solution with a concentration of 15 ppm. Then, the mixture was stirred in the dark during 1 h with the aim to reach the adsorption equilibrium of CIP molecules in catalysts' surface. After that, the visible lamp (λ > 420 nm and 300 W) was switched on and an aliquot was repeatedly taken to obtain the corresponding kinetic curve. The degradation of CIP was followed using a spectrophotometer (SP-830) at 272 nm wavelength, which is the maximum absorbance of CIP molecule.

3. Results and discussion

3.1. Synthesis and characterization

The modified TiO_2 nanoparticles have been synthesized through the hydrolysis of titanium isopropoxide as titanium source at controlled pH and using low amounts of Fe^{3+} and SO_4^{2-} species. The aim of this strategy is to demonstrate that the simultaneous addition of both ions exerts a synergetic influence over the photocatalytic properties in the selected reactions. The quantities of modifiers have been selected in order to ensure the suitable adjustment of the band gap value in the material so that it is active in the visible region of the electromagnetic spectrum and to avoid a high electron-hole recombination rate. It is also desirable to attain the adequate textural properties. The percentage of iron incorporation was established in a theoretical maximum of 1% based on some authors' studies such as Moradi et al., who demonstrated that a high percentage of Fe is detrimental for the photocatalytic activity [18]. This group's studies demonstrated that the degree of particle agglomeration increases with the doping of Fe into the TiO_2 lattice, which is not beneficial for the photocatalytic activity. Regarding the incorporation of sulphur as sulphate ions, a maximum percentage of 1.5% S has been selected bearing in mind a previous report in which similar percentages of sulphur atoms enhanced the selectivity towards the desired product in an oxidation reaction [19]. Other authors have studied the catalytic and photocatalytic activities with the increase of sulphur doping in TiO_2 nanoparticles and have also concluded that a high S-content involves a non-significant enhancement of results or even a worsening of them [20]. Boningari et al. observed a similar behaviour in the photocatalytic degradation of acetaldehyde using materials with high sulphur loadings [21]. In conclusion, the materials studied in this work are based on TiO_2 nanoparticles modified with SO_4^{2-} groups (0.6%S-TiO_2) or Fe^{3+} cations (0.4%Fe-TiO_2) and TiO_2 nanoparticles modified with both Fe^{3+} and SO_4^{2-} ions (1.2%S-0.5%Fe-TiO_2 and 1.5%S-0.8%Fe-TiO_2).

Firstly, all the synthesized photocatalysts were fully characterized. The X-Ray diffraction patterns of 0.4%Fe-TiO_2, 0.6%S-TiO_2, 1.2%S-0.5%Fe-TiO_2 and 1.5%S-0.8%Fe-TiO_2 samples are shown in Fig. 1 and consist of anatase crystal form. The anatase (JCPDS pattern reference card No. 21-1272) [22] crystallizes in an octahedral system and the most intense peaks appear at 2θ values of 25° (101) and 48° (200). The temperature of calcination (400 °C) could mean the appearance of determined peaks of brookite phase as other authors affirm [15]. However, the incorporation of metal and/or non-metal

atoms into TiO_2 lattice, presumably, favours the formation of anatase phase [19]. Some peaks corresponding with (105), (211), (116) and (220) planes are clearly defined in S or Fe-modified TiO_2 samples while in S,Fe-TiO_2 samples the two peaks turn into a broader peak, due to the incorporation of two types of ions and the increase in the amount of them. In addition, no other peak attributed to iron oxide can be detected in the XDR patterns, so we could affirm that all Fe^{3+} ions have incorporated into TiO_2 lattice in substitution of Ti^{4+} cations, due to their similar radii [18]. Zooming in on the most intense peak area, a significant broadening and a slight shift towards higher diffraction angles of the 25° peak are observed the SO_4^{2-} ions are incorporated on TiO_2 in comparison to the sample modified only with Fe that could be indicative of an external incorporation of the SO_4^{2-} ions (see Fig. S1 and Table S1) [23]. According to Williamson and Hall, the diffraction line broadening is due to crystallite size and strain contribution, which is provoked by the crystal imperfection and distortion in powders. The lattice strain can be calculated by the following formula:

$$\varepsilon = \frac{\beta}{4tan\theta}$$

where ε is the lattice strain, β is the full width at half maximum (FWHM) of the (101) diffraction peak and θ is the angle of diffraction. Thus, the lattice strain of 0.4%-Fe-TiO_2 was found to be 0.0178, a lower value in comparison to the values obtained for the materials modified with SO_4^{2-} species, which are superior to 0.02 (see Table S1). The broadening of the (101) peak and the increase in the lattice strain for the materials modified with SO_4^{2-} species imply a loss in the crystallinity and an increase in lattice disorder, due to the incorporation of the SO_4^{2-} ions on the TiO_2 surface.

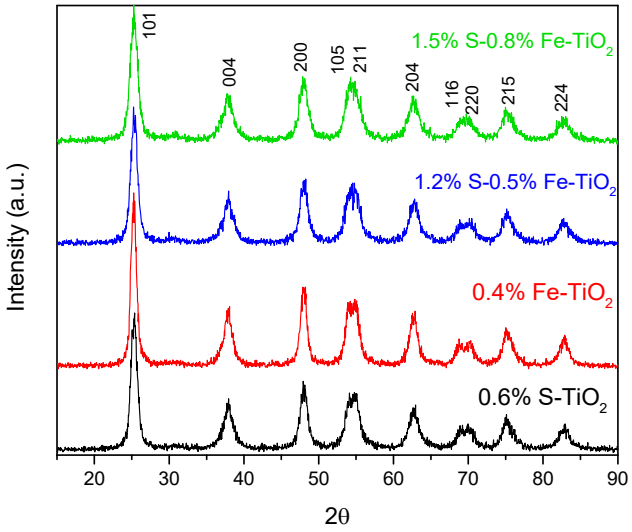

Fig. 1. XRD patterns of the prepared TiO_2 samples.

Textural properties such as surface area, BJH average pore diameter and total pore volume were obtained from nitrogen adsorption and desorption isotherms. As can be seen from Fig. 2a, the samples exhibit similar distributions, well-assigned to TiO_2 nanoparticles [19, 24] and attributed to the mesoporous structure. All materials show type-IV isotherms with a H1 hysteresis loops according to IUPAC classification. However, type-IV isotherms of 0.6% S-TiO_2 and 0.4% Fe-TiO_2 materials show high absorption capability at high relative pressures (around 0.8), which indicates an increase in pore volume values, e.g., 0.6% S-TiO_2 sample with a pore volume of 0.26 $cm^3 \cdot g^{-1}$ (Table 1). The pore size distribution of the TiO_2 nanoparticles was calculated from the adsorption branch of N_2 isotherm by the Barret, Joyner and Halenda (BJH) method (Fig. 2b) and shows a narrow and homogeneous range for the single-modified samples around 9 nm. With the introduction of both species, the pore size distribution decreases until values around 5 nm, which is related to higher superficial BET areas as can be seen in Table 1.

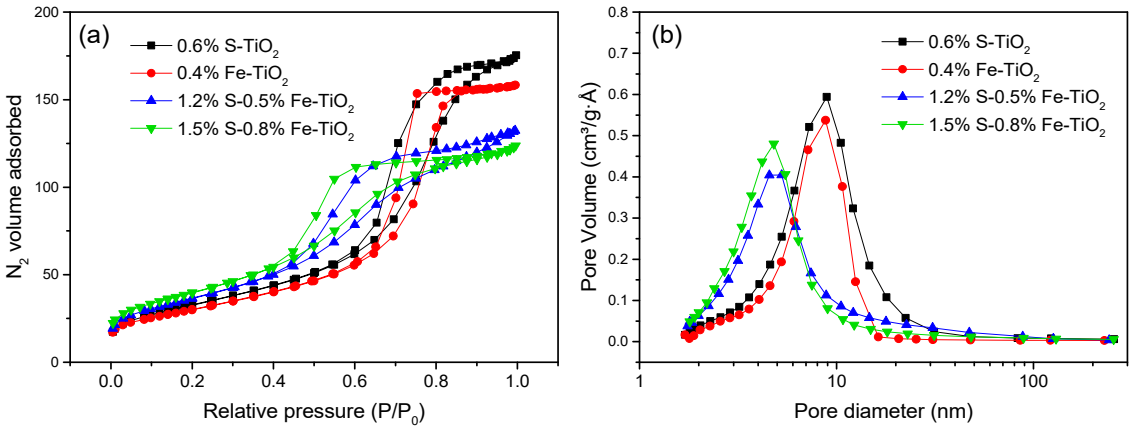

Fig. 2. (a) N_2 adsorption-desorption isotherms and (b) pore size distribution of all prepared TiO_2 samples.

Representative TEM micrographs and the size distribution histograms of all modified TiO_2 nanoparticles are shown in Fig. 3 and Fig. S2. The typical rough morphology of TiO_2 nanoparticles and the formation of mesoporous TiO_2 aggregates can be observed in TEM images. SEM-EDS analysis (Fig. S3) confirms the presence of iron and sulphur in the samples. The length and width ranged from 3-12 nm as the size distribution indicated. For the single-modified samples, a significant aggregation of the 0.4% Fe-TiO_2 nanoparticles is observed with a particle size centred at 7.5 nm, while 0.6% S-TiO_2 sample shows a lower aggregation and a smaller particle size at 6.7 nm. After the incorporation of both ions, 1.2%S-0.5%Fe-TiO_2 and 1.5%S-0.8%Fe-TiO_2 samples maintained a narrow size distribution centred at 6.5 and 5.7 nm, respectively, although the latter shows a slightly wider distribution related to its small size which could provoke a certain aggregation of particles. Scherrer's equation was used to calculate the crystallite size of nanoparticles from the greatest intensity XRD peak, and the results were correlated to the particle sizes calculated from TEM images (Table 1). The SAED patterns (inset in Fig. 3) indicate polycrystalline anatase nature of TiO_2 samples, which is in good agreement with the XRD results.

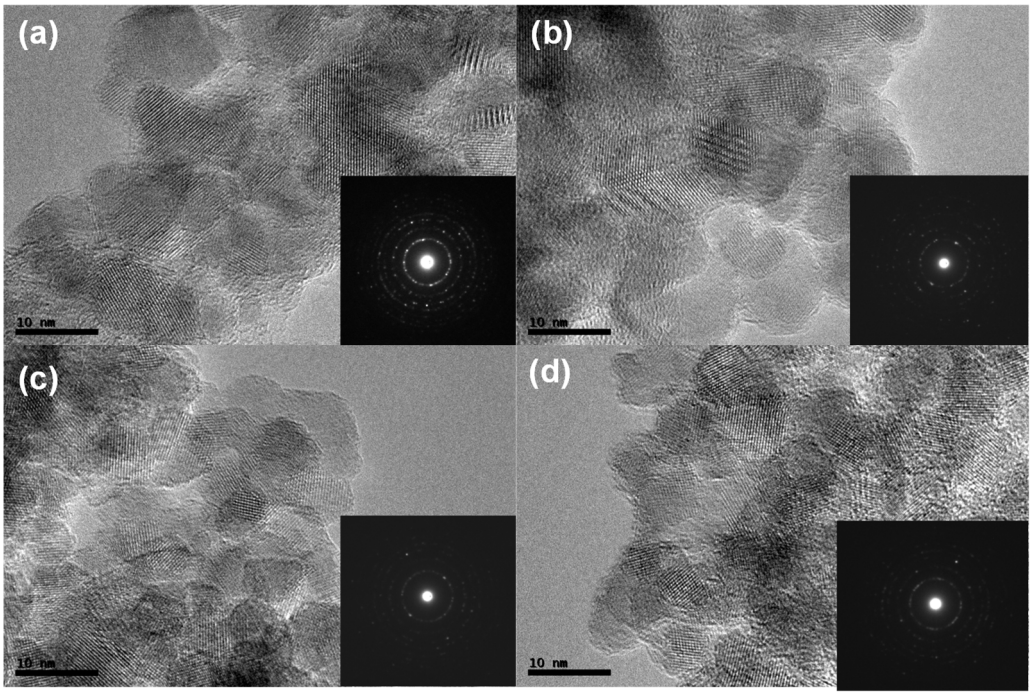

Fig. 3. TEM images and SAED patterns (inset) of a) 0.6%S-TiO_2, b) 0.4%Fe-TiO_2, c) 1.2%S-0.3%Fe-TiO_2, and d) 1.5%S-0.7%Fe-TiO_2 nanoparticles.

Table 1 shows a summary of the textural properties obtained by N_2 isotherms, contains the modifiers' quantities incorporated on titania network obtained by ICP analysis (Fe) and elemental analysis (S) and also includes the particle size and band gap values for all nanoparticles. All synthesized TiO_2 nanoparticles exhibit large surface areas and pore volume values due to the synthesis procedure and the significantly low temperature of calcination. A higher surface area is correlated with a lower particle size as can be observed for 1.5%S-0.8%Fe-TiO_2 sample, while 0.4%Fe-TiO_2 sample possesses the lowest surface area and the highest particle size (9.5 nm). As can be seen, an increase of S content provokes a gradual increase of the BET surface area values (from 128 m^2/g to 144 m^2/g). Christoforidis et al. pointed out that sulphur as dopant limits the formation of anatase phase on TiO_2 nanoparticles, disfavours the formation of large TiO_2 crystallites, and prevents the aggregates [14]. This agrees with TEM analysis and the crystallite size results and justifies the slightly broadening of the most significant peak at 25 2θ observed in XRD pattern (Fig. S1). Therefore, although the ionic radius of the Fe^{3+} is close to Ti^{4+}, a doping with Fe atoms into TiO_2 network also increases the final superficial area BET in samples. Thus, a combination of both ions enhances the textural properties of TiO_2 nanoparticles, which is one of the effective methods for increasing photocatalytic activity.

Table 1. Textural properties of synthesized TiO_2 samples.

Material	S_{BET} ($m^2.g^{-1}$)	V_p[a] ($cm^3.g^{-1}$)	D_p[a] (nm)	Fe Content (%)[b]	S Content (%)[b]	Particle size (nm)[c]	Crystallite size (nm)	Band gap (eV)[d]
0.6%S-TiO_2	128.1	0.26	8.6	-	0.6	8.1	6.7±0.1	3.18
0.4%Fe-TiO_2	107.2	0.24	9.1	0.43	-	9.5	7.9±0.2	2.94
1.2%S-0.5%Fe-TiO_2	133.0	0.21	4.9	0.46	1.2	7.6	6.5±0.2	2.85
1.5%S-0.8%Fe-TiO_2	144.4	0.19	4.7	0.81	1.5	6.9	5.7±0.1	2.73

[a] Total pore volume and pore size as calculated by the BJH method from the adsorption branch of the N_2 isotherm. [b] Fe and S contents were measured by induced coupled plasma atomic emission spectroscopy (ICP-OES) and elemental analysis, respectively. [c] Determined by Scherrer's equation. [d] Calculated by the application of the Kubelka-Munk equation.

The modified TiO_2 nanoparticles were also analyzed by UV-visible Diffuse Reflectance (Fig. 4). All samples show a similar spectrum with a broad band around 320 nm associated with band-band transition, characteristic of these types of materials. The absorbance of S,Fe-TiO_2 nanoparticles in the visible region increases and a red shift in the absorption onset value is observed with increasing modifier percentage (Fig. 4a). Kubelka-Munck equation was used to estimate the band gap energy of the synthesized samples by plotting $(F(R)\cdot E)^{1/2}$ vs E (eV), assuming indirect band gap (see Fig. 4b). The band gap energy values of all TiO_2 samples are summarized in Table 1, and as can be seen, the values decrease with increasing amount of modifier added, from 3.18 eV for 0.6%S-TiO_2 sample until 2.73 eV in the case of 1.5%S-0.8%Fe-TiO_2 sample. It is remarkable that the incorporation of iron doping leads to a narrower band gap value (2.94 eV) in comparison to the modification with sulphate ions (3.18 eV) in the single-modified samples. This may be explained by the incorporation of Fe^{+3} atoms into inner TiO_2 network, which provokes a higher impact than the attachment of SO_4^{2-} groups on the TiO_2 surface.

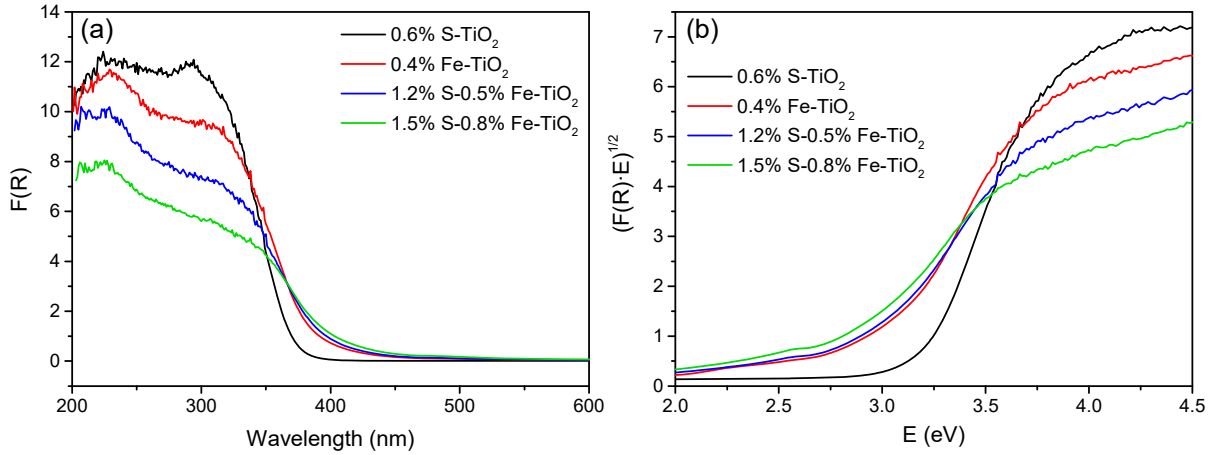

Fig. 4. (a) UV-Visible Diffuse reflectance spectra of TiO_2 samples and (b) plots of Kubelka-Munck equation transformation.

The FTIR spectra of all synthesized TiO_2 nanoparticles were also recorded in the range of 500-4000 cm^{-1} (Fig. 5). All the samples show an intense and broad band around 3300 and at 1630 cm^{-1} due to the surface adsorbed water and hydroxyl groups and correspond to the O-H bending vibration. The intense peak at 500 cm^{-1} is associated to the stretching vibration of Ti-O bond and the Fe-O bond. The bands at 983, 1046, 1124 and 1209 cm^{-1} (shoulder-type the latter peak) are characteristic of a bidentate SO_4^{2-} moiety coordinated to Ti^{4+} of titania's surface. The two bands at 983 and 1046 cm^{-1} are assigned to symmetric and asymmetric stretching vibration of S-O bonds and the signals at 1124 and 1209 cm^{-1} correspond to S=O vibrations [19, 20]. The intensity of these peaks is greater in the sample with the highest sulphur content, 1.5%S-0.8%Fe-TiO_2. Thus, FTIR analysis confirms that SO_4^{2-} ions are anchored on the surface of TiO_2.

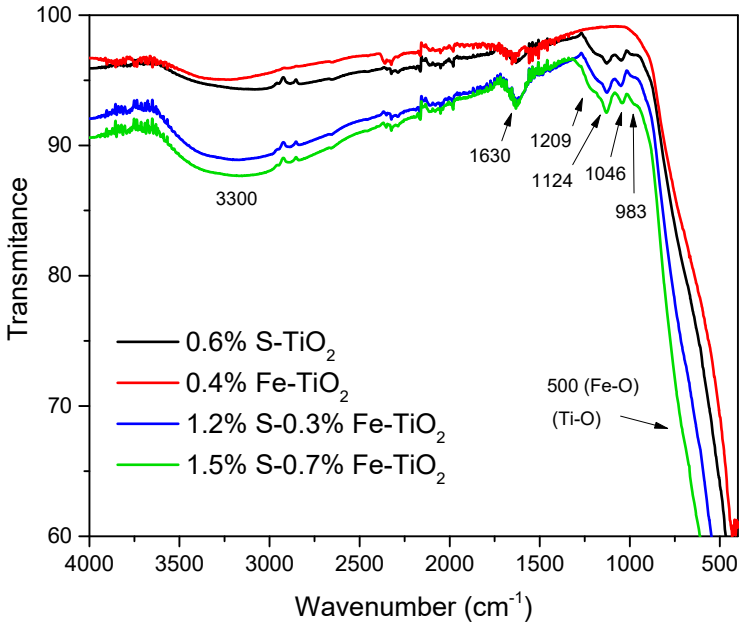

Fig. 5. FTIR spectra of all TiO_2 samples.

Thermogravimetric analysis (TGA) of the S, Fe-TiO_2 samples was carried out with a heating rate of 5 °C/min from 40 °C to 1000 °C under N_2 gas atmosphere and the results are shown in Fig. 6. The TGA-DTG thermograms show a total weight loss of 7 % and 8 % for 1.2%S-0.5%Fe-TiO_2 and 1.5%S-0.8%Fe-TiO_2 samples, respectively, and exhibit three different regions of weight loss in each sample. The first region, located between 40 and 180 °C, is attributed to the removal of the physisorbed water on the nanoparticles' surfaces. The second one is observed from 190 °C to 550 °C and is related to the decomposition of species, such as nitrates and sulphates, used in the synthesis of nanoparticles [25]. Additionally, the intense peak in the DTG curves around 700 °C corresponds to the phase transformation of TiO_2 from anatase to rutile [25].

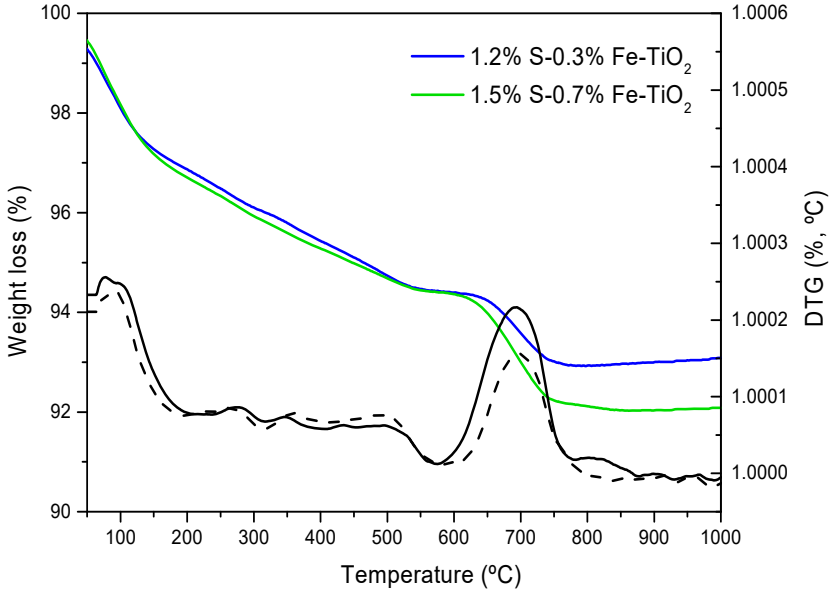

Fig. 6. TGA plots of 1.2%S-0.5%Fe-TiO_2 (blue line) and 1.5%S-0.8%Fe-TiO_2 (green line), and DTG curves of 1.2%S-0.5%Fe-TiO_2 (dotted black line) and 1.5%S-0.8%Fe-TiO_2 (solid black line).

Fig. 7 shows the photoluminescence emission spectra of all synthesized TiO_2 nanoparticles at the excitation wavelength of 250 nm. The spectra of all samples exhibit several peaks where an intense band stands out around 400 nm associated to the band gap transition of TiO_2. In the wavelength range of 450–500 nm the presence of other intense peaks is attributed to the defects/vacancies of oxygen on surface [17]. The PL spectra provides additional information on the separation and recombination process of the electron-hole pair and the efficiency of charge-carrier transfer. As can be observed, a significant drop in the fluorescence intensity of the S,Fe-modified TiO_2 samples is recorded in comparison to the single-modified samples (0.6%S-TiO_2 and 0.4%Fe-TiO_2). This refers to the inhibition of the photo-generated electron recombination that takes place from the conduction band to the valence band in TiO_2-based photocatalysts. Thus, the incorporation of iron and sulphate ions drives to a lower recombination rate and more efficient separation of electron–hole pairs and reveals a higher lifetime of photo-induced charge carriers [19].

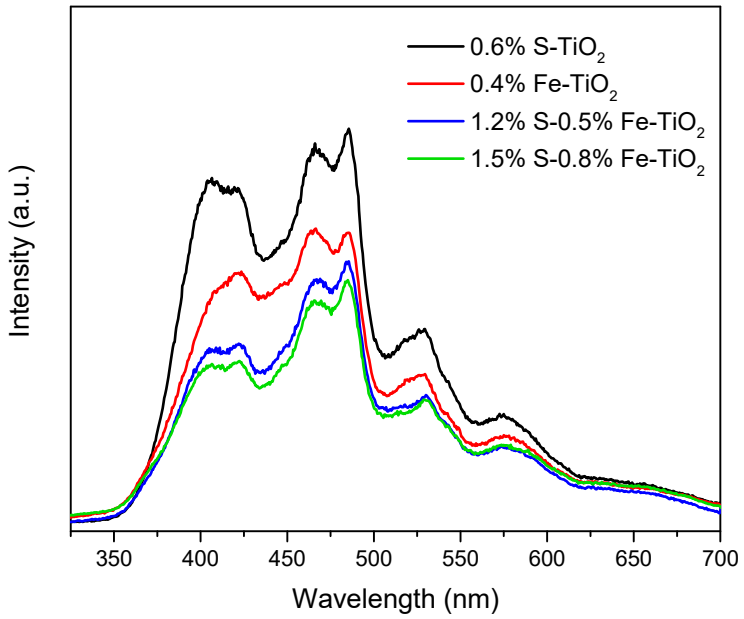

Fig. 7. PL spectra of all synthesized TiO_2 samples.

In order to gain further insight into the chemical composition and chemical states of the synthesized TiO_2 nanoparticles, XPS analysis was performed on the S, Fe-modified samples and the results are shown in Fig. 8. The wide-survey spectra of the analyzed samples showed all the predominant peaks in the samples (Fig. 8a), even the elements with low content. The carbon peak for C 1s located at 284.8 eV is due to the surface adventitious carbon and all electron binding energy were calibrated according to it. A small peak corresponding to N 1s around 400 eV confirms the presence of nitrogen moieties that could be assigned to chemisorbed nitrogen such as N_2 species [26].

The spectra of Ti 2p, S 2p and Fe 2p are separately depicted in Fig. 8 b, c, d, respectively. Fig. 8b shows the two components of Ti 2p, $2p_{3/2}$ and $2p_{1/2}$, at 458.8 eV and 464.6 eV of binding energy, respectively. These peaks were assigned to the oxidation state of titanium Ti^{4+} and correlated with the formation of stoichiometric TiO_2 material in a tetragonal structure since the photopeaks revealed a high symmetry and a lack of shoulders on the lower energy sides [27]. For the S 2p spectra signals were observed around 169 eV (doublet $2p_{3/2}$ at 168.4 eV and $2p_{1/2}$ at 169.6 eV) with the S atom in the (VI) oxidation state corresponding to sulphate groups anchored to the TiO_2 surface coordinating Ti^{4+} species [28].

The XPS signals of Fe 2p are weaker and less clear than the peaks of S 2p or Ti 2p, (Fig. 8d). The main characteristic peaks of Fe 2p, $2p_{3/2}$ and $2p_{1/2}$, appear at 710.1 and 723.7 eV, with the presence of satellite peaks around 716.4 eV, which is consistent with the existence of iron in the positive trivalent form, Fe^{3+}. By comparing the XPS peaks and the obtained oxidation states of Ti^{4+} and Fe^{3+}, we can conclude that the replacement of Ti^{4+} ions from Fe^{3+} occurs and the Fe^{3+} ions can be incorporated into the TiO_2 lattice to form Ti-O-Fe bonds (similar radii, 0.65 Å for Fe^{3+} and 0.606 Å for Ti^{4+} and electronegativity) [29].

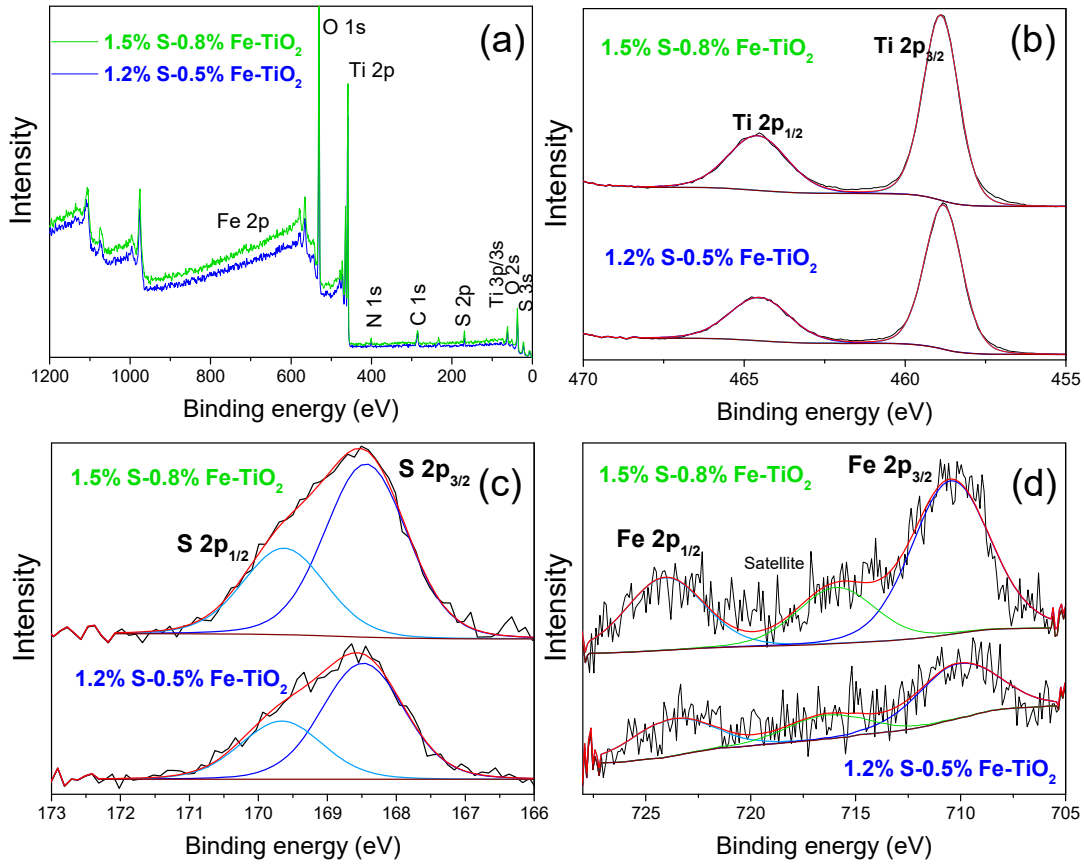

Fig. 8. XPS spectra of the S,Fe-modified TiO_2 samples.

The chemical-physical characterization of the synthesized samples was also studied. The electrochemical properties of our photocatalysts in phosphate buffered saline at pH 7.4 were examined. As an example, 1.5%S-0.8%Fe-TiO_2 material was used to prepare a modified carbon paste electrode (MCPE), immersed in PBS and measured by cyclic voltammetry (CV). Fig. 9 shows cyclic voltammograms for working electrode modified with TiO_2 sample using platinum as a counter and Ag/AgCl(s)/KCl (3M) as a reference

electrode. As can be observed, typical voltammograms for bulk TiO_2 nanoparticles were recorded with a pronounced anodic peak by scanning in the positive direction associated to the electrochemical formation of Ti(III) species in TiO_2 nanoparticles' surfaces. Scanning towards negative potentials it can be inferred that the cathodic peak overlaps with the reduction limit imposed by the solvent. The reactions that take place are: $Ti(IV)(TiO_2) + e^- + H^+$ or $M^+(aq) \rightarrow Ti(III)(TiO_2) + H^+$ or $M^+(TiO_2)$. By increasing the scan rate, the current intensity of voltammograms increases, but the shape is maintained, which reveals a semi diffusion-controlled process by the electrolyte cation insertion into the outer network. Due to this, the TiO_2 modified electrode can be considered as a quasi-reversible system with the presence of reversible surface states.

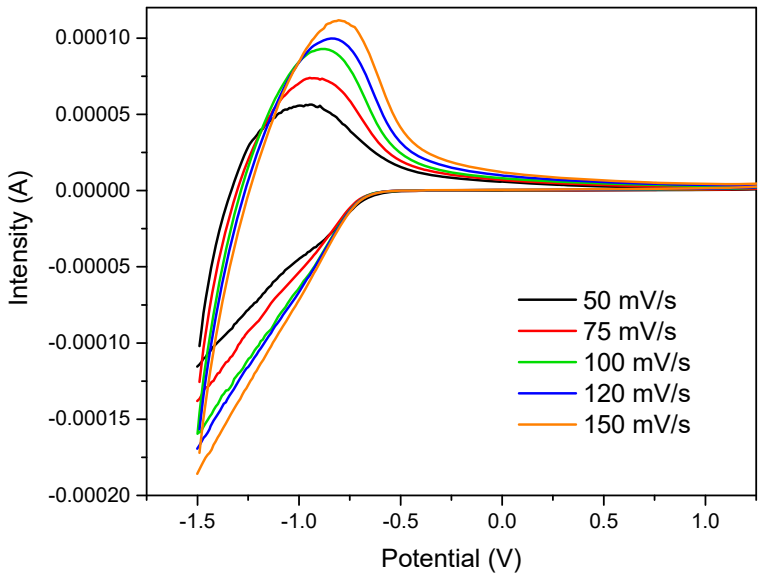

Fig. 9. CV obtained for MCPE with 1.5%S-0.8%Fe-TiO_2 sample immersed in aqueous 0.1 M phosphate buffer with a reversal potential V = -1.5 V at different scan rates vs Ag/AgCl(s)/KCl (3M) as reference electrode.

With the aim to prove the presence of Fe^{3+} cations into TiO_2 network, differential pulse voltammetry (DPV) technique was performed between -0.4 V and 0.5 V and the results shown in Fig. 10. This electrochemical technique is much more sensitive than cyclic voltammetry and allows us to obtain more information of the modified TiO_2 nanoparticles. In this case, 1.2%S-0.5%Fe-TiO_2 and 1.5%S-0.8%Fe-TiO_2 samples were recorded. The cathodic current (from positive to negative potential values) reveals a

reduction peak around 0.09 V consistent with the reduction of Fe^{3+} to Fe^{2+} species. After returning the potential, an anodic peak is clearly observed at potential values around 0.06 V corresponding to the reversible oxidation to Fe^{3+} cations. This behaviour is identical for both S,Fe-modified samples, observing a slight shift and a higher current intensity for the sample with the highest percentage of iron, 1.5%S-0.8%Fe-TiO_2, which supports that the iron loading does not render different structural forms on the titania network.

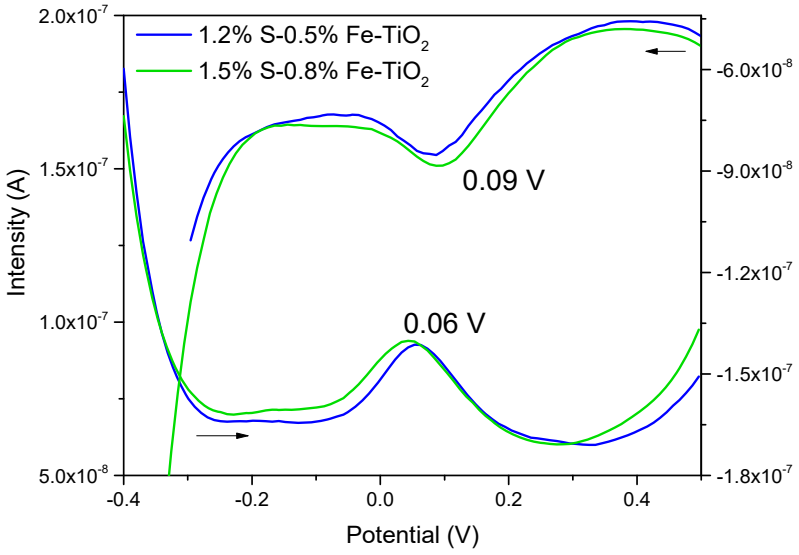

Fig. 10. Anodic and cathodic differential pulse voltammograms (75 mV modulation amplitude) of both S,Fe-modified TiO_2 samples (10 % to graphite) after immersion in phosphate buffer as electrolyte and Ag/AgCl/KCl (3M) as reference electrode.

Electrochemical characterization of the modified TiO_2 nanoparticles was completed by means of cyclic voltammetry measurements using modified carbon paste electrodes (MCPE) as were prepared previously [17, 24]. Thus, the HOMO/LUMO energy levels positions of 1.2%S-0.5%Fe-TiO_2 and 1.5%S-0.8%Fe-TiO_2 materials were calculated based on the following equations:

$$E_{LUMO} = -(E_{red} + 4.4)\ eV$$

$$E_{HOMO} = -(E_{ox} + 4.4)\ eV$$

$$E_{HOMO} = E_{LUMO} - E_g$$

E_{red} and E_{ox} are onset reduction and oxidation potentials, and 4.4 is the energy level of the reference electrode used as standard, Ag/AgCl/KCl (3M). The optical band gap of the samples (E_g) can be calculated through $E_g = 1240/\lambda_g$, where λ_g is the absorption edge of

the material calculated by DRUV spectra (Fig. 3). With all these data, E_{HOMO} and E_{LUMO} are estimated to be -6.70 and -3.68 eV, and -6.64 and -3.71 eV, for 1.2%S-0.5%Fe-TiO_2 and 1.5%S-0.8%Fe-TiO_2, respectively.

3.2. Oxidative desulfurization of dibenzothiophene (DBT).

The catalytic activity of 1.2%S-0.5%Fe-TiO_2 nanoparticles was investigated for DBT removal in 10 mL of model oil containing 100 ppmS at the selected conditions: time 3h, room temperature, 20 mg of catalyst, and in presence of 10 mL of acetonitrile. The experiment results are shown in Table 2. First of all, the result of Entry 1 demonstrated the effect of the addition of acetonitrile to the mixture reaction as multiple studies have pointed out [30, 31]. Dibenzothiophene molecules were extracted from the model oil (n-octane) to the polar phase (acetonitrile) in a percentage of 55.1 %. When hydrogen peroxide was added, only 64.4 % of conversion was reached due to the oxidation of DBT molecules in 3 hours without catalyst. The next experiment was carried out in presence of 1.2%S-0.5%Fe-TiO_2 photocatalyst without visible light irradiation (Entry 3) showing no noteworthy increase in DBT conversion (74.0 %). However, when the visible lamp was turned on, the conversion of DBT was accomplished by above 82 %, in a photooxidation process. The influence of the different catalysts used was also investigated. As shown in Fig. S4, the single-modified samples (0.6%S-TiO_2 and 0.4%Fe-TiO_2) perform a similar pattern in photocatalytic DBT oxidation reaching conversion percentages of up to 70 %. However, the S,Fe-modified samples show greater DBT conversion values than those obtained for single-modified samples up to 82.7 % with 1.2%S-0.5%Fe-TiO_2 sample. These results may be due to the synergetic combination of both ions, a higher amount of sulphate ions in samples, which is beneficial in oxidation of sulphides [19], and a limited percentage of iron in them. In fact, as other studies have confirmed, the photocatalyst with the highest content of iron does not give the best result in DBT oxidation [32]. As Kalantari et al. affirmed, low concentrations of Fe^{3+} trap the electron promoting the reduction of molecular oxygen and, with that, inhibit the recombination electron-hole pairs and increase the photocatalytic activity. Nonetheless, a higher iron concentration decreases the distance between trapping sites and Fe^{3+} cations can act as a recombination centre and reduce the photocatalytic effect.

Table 2. Sulphur removal efficiency with different reaction conditions.

Entry	Catalyst	Visible light irradiation	O/S molar ratio	Conversion (%)[a]	Selectivity (%)[b]
1	-	No	-	55.1	100
2	-	No	4	64.4	100
3	1.2%S-0.5%Fe-TiO_2	No	4	74.0	100
4		Yes	4	82.7	100
5		Yes	6	82.6	100
6		Yes	10	82.5	100

Experimental conditions: 10 mL model oil, 10 mL MeCN, room temperature, 20 mg of 1.2%S-0.5%Fe-TiO_2 catalyst, time = 3 h. [a] Conversion and selectivity determined by GC. [b] Sulphone selectivity checked by ^{1}H NMR (Fig. S5).

The effect of time of light exposition and the catalyst dosage were performed using 1.2%S-0.5%Fe-TiO_2 sample in 20 mL of model mixture (n-octane + acetonitrile) and O/S = 4 molar ratio, and the results are shown in Fig. S6. The catalytic results show that the DBT removal efficiency increases with the reaction time (see Fig. S6a), reaching the maximum of conversion at 3 hours of light exposition. A slight decrease is observed with a prolonged reaction time, which indicates a negligible effect of the time on the DBT desulfurization reaction after 3 h. Fig. S6b shows the effect of the catalyst mass in the photooxidation of DBT. For the indicated material, the conversion increases with its concentration within a limited range from 10 to 20 mg. However, the increase of the catalyst dosage above 20 mg does not mean an increase in DBT conversion. Some authors have found a slight decrease in the activity at higher catalyst masses, which is attributed to a poor dispersion of the catalyst or to the formation of an opaque suspension in the reactor vessel, hindering the adsorption and diffusion of DBT and inhibiting the excitation of the catalyst [33-35].

The addition of an oxidant agent as H_2O_2 has proven to enhance the photooxidation efficiency (see Table 2). With a molar ratio of O/S = 4 the sulphur conversion was 82.7 % but no further improvement was observed when the O/S molar ratio was increased to O/S = 6 or O/S = 10 ratios (Entries 5 and 6, respectively). Several reasons can explain this

behaviour, the oxidation process can be hampered by the presence of water in high quantity which would decrease the emulsion properties of the fluid [30, 36], or by the addition of H_2O_2 which may form a liquid film on the catalyst surface hindering DBT adsorption to the active sites [37] and deactivating the material surface [38]. Other authors pointed out that the hydroxyl radicals generated when H_2O_2 is exposed to light can be consumed by H_2O_2 molecules themselves as described in the following reaction: $H_2O_2 + \cdot OH \rightarrow H_2O + O_2^- + H^+$ [30]. For all these reasons, we tested the use of a promoter or co-oxidant to enhance the DBT conversion. In the presence of hydrogen peroxide, peroxyacetic acid would be produced, which would coordinate to the Fe or/and Ti atoms in the materials to form the so-called peroxometallic complexes and generate reactive oxygen species on the catalyst surface [33]. As can be seen in Fig. 11 the effect of adding acetic acid to the mixture reaction is beneficial since an increase of acetic acid means an increase of DBT conversion. The best result was 91.3 % of conversion which was reached with a O/S ratio of 10 and 20 μL of acetic acid. Comparing with other reported results, Kalantari et al. obtained 40.3 % of DBT conversion in presence of N doped TiO_2 nanoparticles [39] and 59.8 % in the case of co-doped Fe-N-TiO_2 nanoparticles [32]. More recently, Guo et al. have demonstrated that dye-sensitized TiO_2@SBA-15 composites showed a higher photocatalytic activity than the unsensitised ones, obtaining 96.1 % of DBT conversion [34].

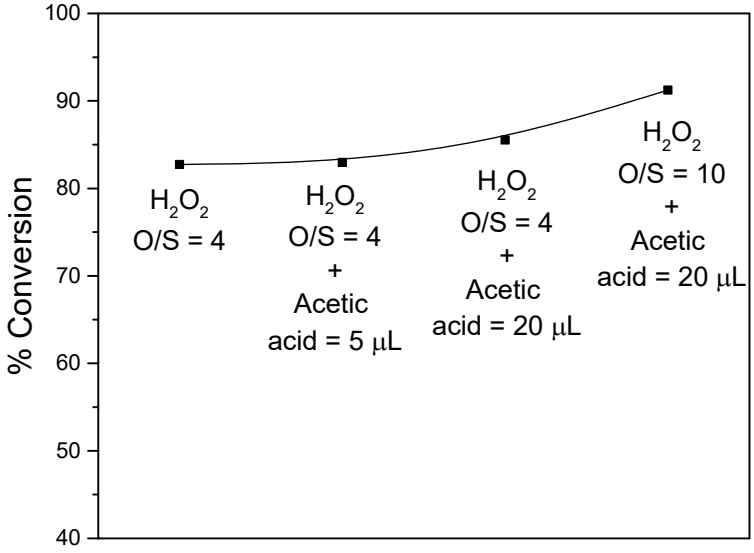

Fig. 11. Effect of the use of H_2O_2 and acetic acid as oxidant agents. Conditions: 20 mg of 1.2%S-0.5%Fe-TiO_2 catalyst, 10 mL n-octane, 10 mL acetonitrile, room temperature, 3 h of visible lamp.

3.3. Photocatalytic degradation of ciprofloxacin under visible light

Degradation of ciprofloxacin drug was evaluated in the presence of the TiO_2 photocatalysts under visible light irradiation using 8 mg of photocatalyst and 20 mL of CIP solution with 15 ppm of concentration and the results were depicted in Fig. 12. Previously, the catalyst was mixed and stirred with the aqueous solution of ciprofloxacin for 60 minutes to ensure the adsorption equilibrium on the photocatalysts' surface. Fig. 12a shows the quantity of drug adsorbed, which is similar to samples doped with iron (around 21.5 %) and slightly lower than S-modified TiO_2 (14 %). Two additional experiments with the S,Fe samples were performed using 20 mg of photocatalyst and the same CIP solution volume resulting a concentration of 1 g/L and provoking an increase in drug quantity adsorbed (around 36 %). Additionally, as we demonstrated in previous reports, the photolysis of ciprofloxacin molecules was practically negligible under similar experimental conditions in absence of the catalyst [19].

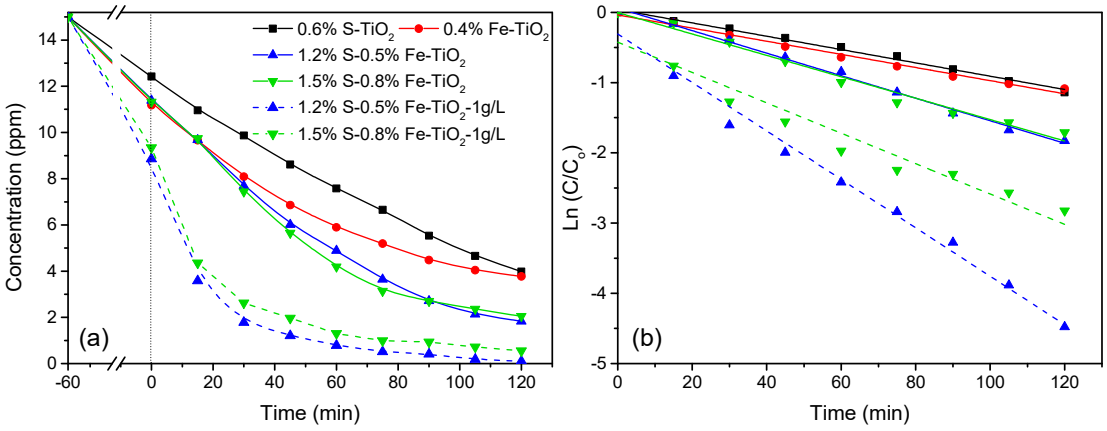

Fig. 12. Degradation kinetics of ciprofloxacin in terms of (a) concentration and (b) ln(C/C_o) versus time in minutes.

As can be seen in Fig. 12a, both S,Fe-TiO_2 photocatalysts have a higher degradation activity than that achieved for 0.6% S-TiO_2 or 0.4% Fe-TiO_2 samples under visible light irradiation. Thus, 0.6%-TiO_2 and 0.4%-TiO_2 nanoparticles achieved around 70 % of degradation at 2 hours of starting the experiment, while S,Fe-modified samples reached an elimination above 84 % at the same time, indicating a synergetic effect of the

incorporation of sulphate and iron ions to TiO_2. With the aim of ensuring the complete degradation of CIP molecules, the ratio photocatalyst/volume was increased to 1 g/L for the S,Fe-TiO_2 samples. The best result was obtained for the 1.2%S-0.5%Fe-TiO_2 photocatalyst, which was capable of degrading almost completely the 100 % of CIP pollutant in 90 minutes. According to the data plotted in Fig. 12b, the photocatalytic degradation of ciprofloxacin drug followed a pseudo-first-order kinetic for all the prepared TiO_2 samples. The kinetic constants obtained in each experiment are given in Table 3, where the promising results for S,Fe-TiO_2 samples are corroborated, reaching a rate of 0.034 min^{-1} for 1.2%S-0.5%Fe-TiO_2 photocatalyst, which is nearly 4 times higher than the results obtained for single-modified samples. The results obtained by other comparative systems reported are shown in Table 3.

Table 3. Kinetic constants of pseudo-first order reaction of different catalysts for photocatalytic degradation of CIP.

Catalyst	***k* (min^{-1})**	**Catalyst dosage (g/L)**	**CIP concentration (ppm)**	**Reference**
0.4%Fe-TiO_2	0.009	0.4	15	This work
0.6%S-TiO_2	0.009	0.4	15	This work
1.2%S-0.5%Fe-TiO_2	0.016	0.4	15	This work
1.5%S-0.8%Fe-TiO_2	0.015	0.4	15	This work
1.2%S-0.5%Fe-TiO_2	0.034	1	15	This work
1.5%S-0.8%Fe-TiO_2	0.022	1	15	This work
1%Ce-TiO_2	0.0266	0.5	10	[40]
1%B-TiO_2	0.0249	1	10	[40]
NaCl/TiO_2	0.0099	1	10	[41]
N,S-TiO_2	0.0115	0.5	10	[42]
N-TiO_2	0.002	0.5	15	[43]
2.5%N-0.5%Fe-TiO_2	0.0038	1	20	[26]
2.5%N-1%Fe-TiO_2	0.0044	1	20	[26]
Ti^{3+}/N-TiO_2	0.0132	0.43	4.5	[44]

With the aim of justifying the different photocatalytic behaviour between the two S,Fe-modified TiO_2 samples in the DBT oxidation and CIP degradation, electrochemistry measurements have been employed. Linear sweep voltammetry (LSV) was the selected technique to measure the photoelectrochemical behaviour of both S,Fe-TiO_2 catalysts modified with carbon paste electrodes (MCPE). Fig. 13 shows the voltammograms obtained in presence and in absence of visible light and by using Na_2SO_4 0.2 M as an electrolyte. The increase observed in the photocurrent towards more positive potential values is related to the higher and effective charge density and the lower electron-hole recombination. Iron doping seems to act as an electron-hole trap, and it inhibits the recombination rate of the photogenerated electrons. Besides, the replacement of Ti^{+4} by Fe^{+3} ions leads to Fe^{+3} states that are located near to the conduction level [32], which results in the enhancement in the photocurrent [45]. Fig. 13 shows a better performance of 1.2%S-0.5%Fe-TiO_2 in terms of enhancement of photocurrent than 1.5%S-0.8%Fe-TiO_2 photocatalyst both in darkness and under visible light irradiation. These results validate the better catalytic and photocatalytic behaviour of 1.2%S-0.5%Fe-TiO_2 sample in comparison to 1.5%S-0.8%Fe-TiO_2, despite the lower band gap value that the latter possesses.

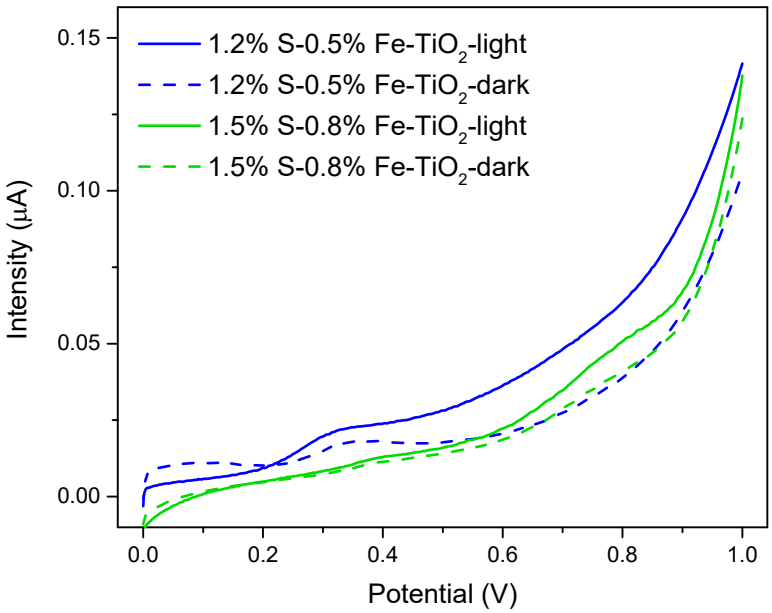

Fig. 13. Linear sweep voltammetry of both S,Fe-modified TiO_2 samples after immersion in Na_2SO_4 0.2 M and Ag/AgCl/KCl (3M) as reference electrode.

To evaluate the resistance against electron transfer, cyclic voltammetry and electrochemical impedance spectroscopy (EIS) measurements of the samples modified with sulphate and iron were also conducted and the results are shown in Fig. 14. The measurements were performed by using the modified sample with carbon paste electrodes (MCPE) immersed in Na_2SO_4 0.2 M and by using $[Fe(CN)_6]^{3-}$ 5 mM as a probe molecule. Cyclic voltammograms (Fig. 14a) show how the modification of the carbon electrode resulted in a higher electron transfer mobility, i.e., S,Fe-modified TiO_2 nanoparticles electrodes improve the electron transfer since their cyclic voltammograms show a lower peak potential separation (ΔE) and a narrower intensity peak. Regarding the EIS results (Fig. 14b), in the Nyquist plot, the semicircles at high frequencies and medium frequencies are attributed to the charge-transfer resistance on the electrode-electrolyte interface and the straight sloping designated to Warburg impedance is attributed to diffusional impedance. Compared to bare carbon paste electrode (CPE), S,Fe-modified TiO_2 nanoparticles show a smaller internal resistance, which means a better charge transport. Among them, 1.2%S-0.5%Fe-TiO_2 catalyst presents the best performance in terms of charge transfer and improved photoactivity. According to the modified Randles equivalent circuit (inset in Fig. 14b), the electron transfer resistance (R_{et}) for bare CPE is about 11.5 kΩ, for 1.5%S-0.8%Fe-TiO_2 catalyst is about 10.2 kΩ and for 1.2%S-0.5%Fe-TiO_2 catalyst is about 9.7 kΩ, revealing a better electronic and ionic conduction in the latter, which demonstrates the best electrochemical behaviour and photocatalytic activity of this catalyst.

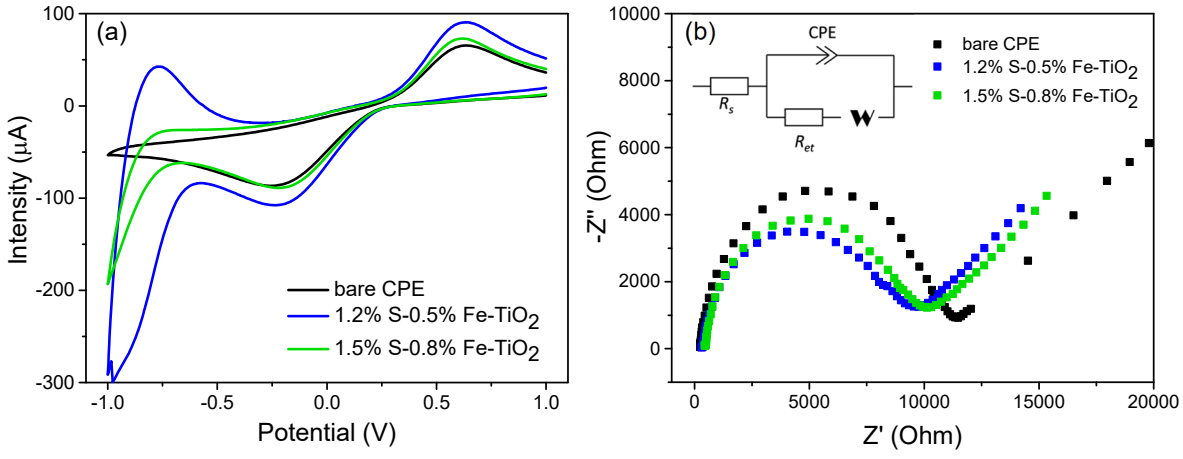

Fig. 14. (a) CV and (b) EIS measurements of bare and modified carbon paste electrodes after immersion in Na_2SO_4 0.2 M with Ag/AgCl/KCl (3M) as reference electrode and $[Fe(CN)_6]^{3-}$ 5 mM as a probe molecule.

3.4. Mechanism proposal

In agreement with the results obtained, a probable mechanism for the photocatalytic removal of DBT and CIP pollutants is proposed in Scheme 1. The process starts with the light irradiation to the photocatalyst that, after visible absorption, promotes the electrons from valence band to conduction band generating positives holes in the first one. Electrons in conduction band are used for reducing molecular oxygen to give superoxide radicals. It has been demonstrated that dibenzothiophene molecules can be oxidized to dibenzothiophene sulphone by both photogenerated positive holes and superoxide radicals [46]. Similarly, ciprofloxacin molecule has been proven to be degraded by these species, but hydroxyl radicals also play an important role in the removal of CIP [44]. In the case of DBT removal, hydrogen peroxide can be reduced to form hydroxyl radicals which play an important role in DBT photooxidation as reactive oxidizing agents like other studies have confirmed [47].

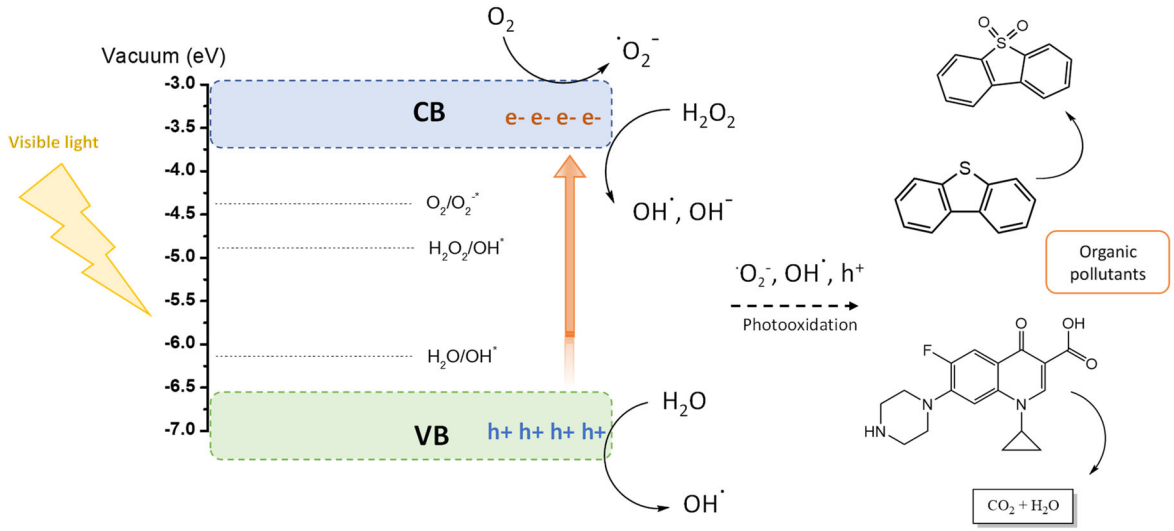

Scheme 1. Schematic diagram for the photocatalytic removal of organic pollutants.

Additionally, to investigate the nature of the species generated during photocatalytic experiments, a degradation kinetic of ciprofloxacin was performed and several aliquots were taken at certain times and analyzed by cyclic voltammetry. As shown in Fig. S7, before the photodegradation process starts, a clear oxidation peak appears around -0.7 V which can be associated to ciprofloxacin molecules. The intensity of this peak

decreases over time when the degradation takes place while, at the same time, the appearance of new species with less negative reduction peaks is observed, that can be justified by the formation of more oxidized species after the photooxidation process to which the starting species have been subjected.

For a deeper understanding of the photocatalytic degradation pathways of ciprofloxacin by of 1.2%S-0.5%Fe-TiO_2 material the generated intermediate products during the photocatalytic process under the optimum conditions were examined by HPLC/MS. Fig. S8 shows the peaks obtained by HPLC analysis and the molecular weight of intermediate products, respectively. Based on the experimental results and the literature, the possible degradation pathway of CIP molecules was proposed as following. In the first place, defluorination process results in the replacement of F^- with OH^- (*m/z* 328) [48], which evolves into *m/z* of 301 through decarboxylation in quinoline moieties. The next pathway could go forward through two possibilities: via the elimination of one of the hydroxyl groups (*m/z* 285) or through opening piperazine ring (*m/z* 275) [40]. The first one could lose simultaneously another hydroxyl and carbonyl groups and open piperazine ring to form *m/z* of 229 and the latter compound appears with the unsaturation of two bonds in piperazine moiety and hydroxyl loss (*m/z* 255). Both compounds *m/z* 255 and 229 evolve into the same quinoline ring with *m/z* of 131, which leads into *m/z* of 121 through an opening of the right ring. Finally, it leads to compounds with lower molecular weight until the complete mineralization into CO_2 + H_2O (Fig. 15).

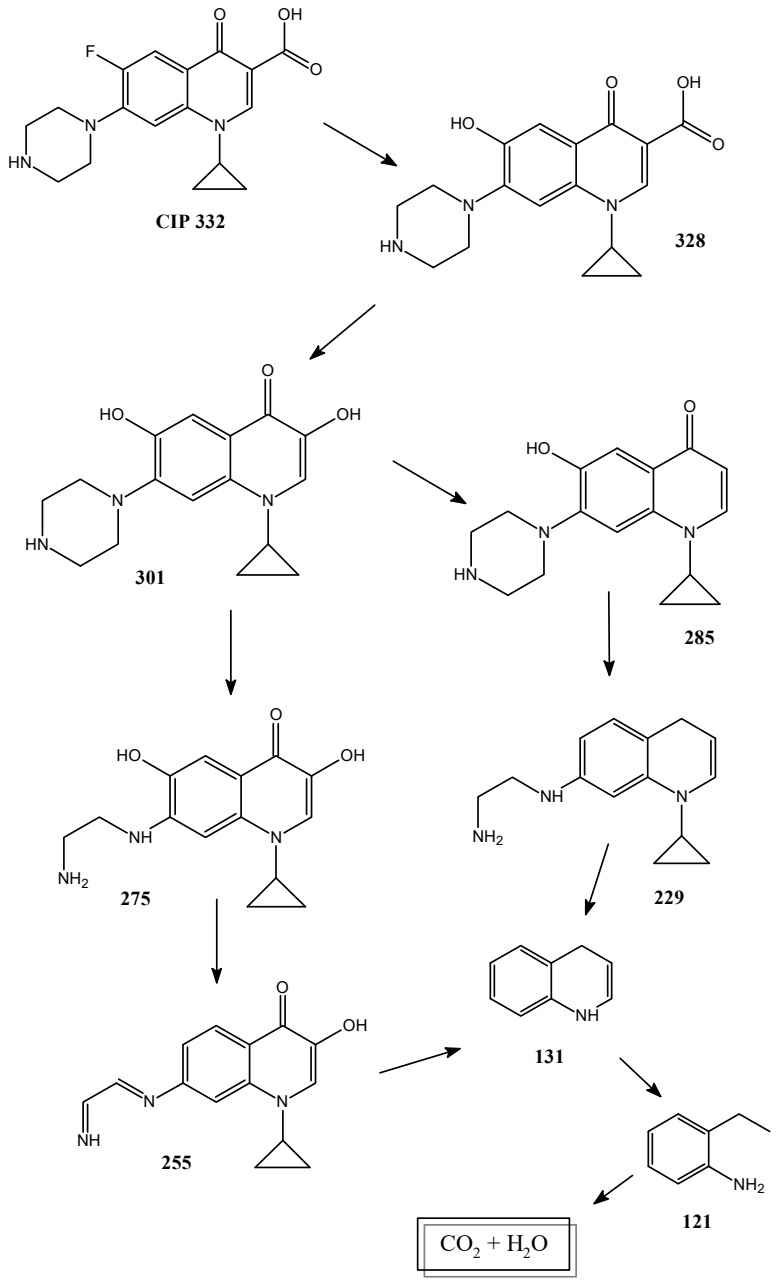

Fig. 15. Proposal for the CIP photodegradation mechanism.

3.5. Photocatalytic stability and catalyst' recycling.

Recyclability is a crucial property of the photocatalyst, which directly affects the practical application of it. To investigate the stability of the best catalyst, 1.2%S-0.5%Fe-TiO_2 sample, the DBT and CIP photocatalytic experiments were repeated for several cycles. After each photodegradation reaction, the selected photocatalyst was recycled through filtration, washing with water and ethanol, and drying under vacuum for the next cycle. As shown in Fig. S9, the activity of 1.2%S-0.5%Fe-TiO_2 was preserved after various cycles for both photocatalytic reactions, revealing the good stability and recyclability of our

modified TiO_2 nanoparticles. The reused 1.2%S-0.5%Fe-TiO_2 catalyst was analyzed by FTIR and differential pulse voltammetry (DPV) studies and the results are shown in Fig. S9 c, d, respectively. FTIR spectrum of the recovered materials shows the presence of the bands associated to sulphate groups and DPV curves confirm the presence of Fe^{3+} ions in titania network. This highly sensitive technique allows us to detect a slight shift to more negative potential values, which could be assigned to the peroxometallic complexes formed on the catalyst surface due to the presence of oxidant species in the reaction medium and that we inferred in the DBT oxidation discussion [49].

4. Conclusions.

Photocatalysts based on the modification of TiO_2 nanoparticles with Fe^{3+} and SO_4^{2-} ions have been prepared and have proved their efficiency for the photocatalytic removal of two types of organic pollutants under visible light irradiation. The suitable adjustment of the amounts of doping agents has allowed for designing multifunctional photocatalysts which are active in the visible region of the spectrum and show an enhanced photocatalytic activity. Among them, 1.2%S-0.5%Fe-TiO_2 photocatalyst stands out by a lower recombination rate and more efficient separation of electron–hole pairs and reveals a higher lifetime of photo-induced charge carriers, which are corroborated by optical and electrochemical techniques, such as photoluminescence and electrochemical impedance spectroscopy (EIS). 1.2%S-0.5%Fe-TiO_2 photocatalyst accomplishes a 91.3 % of DBT conversion under optimized conditions, degrades CIP molecules 4 times faster than single-modified TiO_2 nanoparticles, and maintains its stability under several cycles. Cyclic voltammetry and HPLC-MS measurements confirm the formation of oxidized species after the photooxidation process to which the starting species were subjected.

Acknowledgements

We gratefully acknowledge financial support from the Ministerio de Ciencia e Innovación, MICINN (project RTI2018-094322-B-I00).

References

[1] X. Zhou, T. Wang, H. Liu, X. Gao, C. Wang, G. Wang, Desulfurization through Photocatalytic Oxidation: A Critical Review, ChemSusChem, 14 (2021) 492-511.

[2] A. Stanislaus, A. Marafi, M.S. Rana, Recent advances in the science and technology of ultra low sulfur diesel (ULSD) production, Catal. Today, 153 (2010) 1-68.
[3] S. Li, N. Mominou, Z. Wang, L. Liu, L. Wang, Ultra-deep Desulfurization of Gasoline with CuW/TiO2–GO through Photocatalytic Oxidation, Energ. Fuels, 30 (2016) 962-967.
[4] B. Li, H. Song, F. Han, L. Wei, Photocatalytic oxidative desulfurization and denitrogenation for fuels in ambient air over Ti3C2/g-C3N4 composites under visible light irradiation, Appl Catal B-Environ, 269 (2020) 118845.
[5] X. Li, Z. Zhang, C. Yao, X. Lu, X. Zhao, C. Ni, Attapulgite-CeO2/MoS2 ternary nanocomposite for photocatalytic oxidative desulfurization, Appl. Surf. Sci., 364 (2016) 589-596.
[6] X. Li, W. Zhu, X. Lu, S. Zuo, C. Yao, C. Ni, Integrated nanostructures of CeO2/attapulgite/g-C3N4 as efficient catalyst for photocatalytic desulfurization: Mechanism, kinetics and influencing factors, Chem. Eng. J., 326 (2017) 87-98.
[7] M. Bagheri, M.Y. Masoomi, A. Morsali, A MoO3–Metal–Organic Framework Composite as a Simultaneous Photocatalyst and Catalyst in the PODS Process of Light Oil, ACS Catalysis, 7 (2017) 6949-6956.
[8] X. Li, F. Li, X. Lu, S. Zuo, Z. Li, C. Yao, C. Ni, Microwave hydrothermal synthesis of BiP1−xVxO4/attapulgite nanocomposite with efficient photocatalytic performance for deep desulfurization, Powder Technol., 327 (2018) 467-475.
[9] M. Gavrilescu, K. Demnerová, J. Aamand, S. Agathos, F. Fava, Emerging pollutants in the environment: present and future challenges in biomonitoring, ecological risks and bioremediation, N. Biotechnol, 32 (2015) 147-156.
[10] S. Lacorte, S. Luis, C. Gómez-Canela, T. Sala-Comorera, A. Courtier, B. Roig, A.M. Oliveira-Brett, C. Joannis-Cassan, J.I. Aragonés, L. Poggio, T. Noguer, L. Lima, C. Barata, C. Calas-Blanchard, Pharmaceuticals released from senior residences: occurrence and risk evaluation, Environ. Sci. Pollut. Res, 25 (2018) 6095-6106.
[11] M. Patel, R. Kumar, K. Kishor, T. Mlsna, C.U. Pittman, D. Mohan, Pharmaceuticals of Emerging Concern in Aquatic Systems: Chemistry, Occurrence, Effects, and Removal Methods, Chem. Rev, 119 (2019) 3510-3673.
[12] W. Li, L. Xie, L. Zhou, J. Ochoa-Lozano, C. Li, X. Chai, A systemic study on Gd, Fe and N co-doped TiO2 nanomaterials for enhanced photocatalytic activity under visible light irradiation, Ceram. Int, 46 (2020) 24744-24752.
[13] Y. Niu, M. Xing, J. Zhang, B. Tian, Visible light activated sulfur and iron co-doped TiO2 photocatalyst for the photocatalytic degradation of phenol, Catal. Today, 201 (2013) 159-166.
[14] K.C. Christoforidis, S.J.A. Figueroa, M. Fernández-García, Iron–sulfur codoped TiO2 anatase nano-materials: UV and sunlight activity for toluene degradation, Appl. Catal. B-Environ, 117-118 (2012) 310-316.
[15] W. He, Z. Fang, K. Zhang, X. Li, D. Ji, X. Jiang, C. Qiu, K. Guo, Continuous synthesis of a co-doped TiO2 photocatalyst and its enhanced visible light catalytic activity using a photocatalysis microreactor, RSC Adv, 5 (2015) 54853-54860.
[16] F.J.A. Villaluz, M.D.G. de Luna, J.I. Colades, S. Garcia-Segura, M.-C. Lu, Removal of 4-chlorophenol by visible-light photocatalysis using ammonium iron(II) sulfate-doped nano-titania, Process Saf. Environ, 125 (2019) 121-128.
[17] J. Ortiz-Bustos, M. Fajardo, I. del Hierro, Y. Pérez, Versatile titanium dioxide nanoparticles prepared by surface-grown polymerization of polyethylenimine for photodegradation and catalytic CC bond forming reactions, Mol. Catal., 475 (2019) 110501.
[18] H. Moradi, A. Eshaghi, S.R. Hosseini, K. Ghani, Fabrication of Fe-doped TiO2 nanoparticles and investigation of photocatalytic decolorization of reactive red 198 under visible light irradiation, Ultrason. Sonochem, 32 (2016) 314-319.
[19] J. Ortiz-Bustos, S. Gómez-Ruiz, J. Mazarío, M.E. Domine, I. del Hierro, Y. Pérez, Copper and sulphur co-doped titanium oxide nanoparticles with enhanced catalytic and photocatalytic properties, Catal. Sci. Technol, 10 (2020) 6511-6524.

[20] Y. Shao, W. Du, Z. Gao, K. Sun, Z. Zhang, Q. Li, L. Zhang, S. Zhang, Q. Liu, X. Hu, Sulfated TiO2 nanosheets catalyzing conversion of biomass derivatives: influences of the sulfation on distribution of Brønsted and Lewis acidic sites, J. Chem. Technol. Biotechnol, 95 (2020) 1337-1347.
[21] T. Boningari, S.N.R. Inturi, M. Suidan, P.G. Smirniotis, Novel one-step synthesis of sulfur doped-TiO2 by flame spray pyrolysis for visible light photocatalytic degradation of acetaldehyde, Chem. Eng. J, 339 (2018) 249-258.
[22] D. Reyes-Coronado, G. Rodríguez-Gattorno, M.E. Espinosa-Pesqueira, C. Cab, R. de Coss, G. Oskam, Phase-pure TiO(2) nanoparticles: anatase, brookite and rutile, Nanotechnology, 19 (2008) 145605.
[23] L.G. Devi, R. Kavitha, Enhanced photocatalytic activity of sulfur doped TiO2 for the decomposition of phenol: A new insight into the bulk and surface modification, Mater. Chem. Phys, 143 (2014) 1300-1308.
[24] J. Ortiz-Bustos, I.d. Hierro, A. Sánchez-Ruiz, J.C. García-Martínez, Y. Pérez, Tuning of type-I and type-II mechanisms for visible light degradation in tris(styryl)benzene-sensitized TiO2 nanoparticles, Dyes Pigments, 184 (2021) 108802.
[25] D. Wang, L. Xiao, Q. Luo, X. Li, J. An, Y. Duan, Highly efficient visible light TiO2 photocatalyst prepared by sol–gel method at temperatures lower than 300°C, J. Hazard. Mater, 192 (2011) 150-159.
[26] T. Suwannaruang, J.P. Hildebrand, D.H. Taffa, M. Wark, K. Kamonsuangkasem, P. Chirawatkul, K. Wantala, Visible light-induced degradation of antibiotic ciprofloxacin over Fe–N–TiO2 mesoporous photocatalyst with anatase/rutile/brookite nanocrystal mixture, J. Photochem. Photobiol. A, 391 (2020) 112371.
[27] C. Kapridaki, N. Xynidis, E. Vazgiouraki, N. Kallithrakas-Kontos, P. Maravelaki-Kalaitzaki, Characterization of Photoactive Fe-TiO2 Lime Coatings for Building Protection: The Role of Iron Content, Materials, 12 (2019) 1847.
[28] G. Colón, M.C. Hidalgo, J.A. Navío, A. Kubacka, M. Fernández-García, Influence of sulfur on the structural, surface properties and photocatalytic activity of sulfated TiO2, Appl. Catal. B-Environ, 90 (2009) 633-641.
[29] J. Fang, W. Liu, F. Yu, F. Qin, M. Wang, K. Zhang, Y. Lai, Fe, S co-doped anatase TiO2 nanotubes as anodes with improved electrochemical performance for lithium ion batteries, RSC Adv, 6 (2016) 70133-70140.
[30] G. Dedual, M.J. MacDonald, A. Alshareef, Z. Wu, D.C.W. Tsang, A.C.K. Yip, Requirements for effective photocatalytic oxidative desulfurization of a thiophene-containing solution using TiO2, J. Environ. Chem. Eng, 2 (2014) 1947-1955.
[31] D. Zheng, W. Zhu, S. Xun, M. Zhou, M. Zhang, W. Jiang, Y. Qin, H. Li, Deep oxidative desulfurization of dibenzothiophene using low-temperature-mediated titanium dioxide catalyst in ionic liquids, Fuel, 159 (2015) 446-453.
[32] K. Kalantari, M. Kalbasi, M. Sohrabi, S.J. Royaee, Enhancing the photocatalytic oxidation of dibenzothiophene using visible light responsive Fe and N co-doped TiO2 nanoparticles, Ceram. Int, 43 (2017) 973-981.
[33] U. Arellano, J.A. Wang, M.T. Timko, L.F. Chen, S.P. Paredes Carrera, M. Asomoza, O.A. González Vargas, M.E. Llanos, Oxidative removal of dibenzothiophene in a biphasic system using sol–gel FeTiO2 catalysts and H2O2 promoted with acetic acid, Fuel, 126 (2014) 16-25.
[34] G. Guo, H. Guo, F. Wang, L.J. France, W. Yang, Z. Mei, Y. Yu, Dye-sensitized TiO2@SBA-15 composites: Preparation and their application in photocatalytic desulfurization, Green Energy Environ, 5 (2020) 114-120.
[35] R. Liu, J. Zhang, Z. Xu, D. Zhao, S. Sun, Visible light photocatalytic oxidative desulfurization using Ti-MCM-41-loaded iron phthalocyanine combined with ionic liquid extraction, J. Mater. Sci, 53 (2018) 4927-4938.

[36] W. Abdul-Kadhim, M.A. Deraman, S.B. Abdullah, S.N. Tajuddin, M.M. Yusoff, Y.H. Taufiq-Yap, M.H.A. Rahim, Efficient and reusable iron-zinc oxide catalyst for oxidative desulfurization of model fuel, J. Environ. Chem. Eng., 5 (2017) 1645-1656.
[37] L. Li, J. Zhang, C. Shen, Y. Wang, G. Luo, Oxidative desulfurization of model fuels with pure nano-TiO2 as catalyst directly without UV irradiation, Fuel, 167 (2016) 9-16.
[38] J. Zhang, D. Zhao, J. Wang, L. Yang, Photocatalytic oxidation of dibenzothiophene using TiO2/bamboo charcoal, J. Mater. Sci, 44 (2009) 3112-3117.
[39] K. Kalantari, M. Kalbasi, M. Sohrabi, S.J. Royaee, Synthesis and characterization of N-doped TiO2 nanoparticles and their application in photocatalytic oxidation of dibenzothiophene under visible light, Ceram. Int, 42 (2016) 14834-14842.
[40] M. Manasa, P.R. Chandewar, H. Mahalingam, Photocatalytic degradation of ciprofloxacin & norfloxacin and disinfection studies under solar light using boron & cerium doped TiO2 catalysts synthesized by green EDTA-citrate method, Catal. Today, (2020).
[41] X. Liu, P. Lv, G. Yao, C. Ma, Y. Tang, Y. Wu, P. Huo, J. Pan, W. Shi, Y. Yan, Selective degradation of ciprofloxacin with modified NaCl/TiO2 photocatalyst by surface molecular imprinted technology, Colloids Surf. A Physicochem. Eng. Asp, 441 (2014) 420-426.
[42] L.T. Nguyen, H.T. Nguyen, T.-D. Pham, T.D. Tran, H.T. Chu, H.T. Dang, V.-H. Nguyen, K.M. Nguyen, T.T. Pham, B. Van der Bruggen, UV–Visible Light Driven Photocatalytic Degradation of Ciprofloxacin by N,S Co-doped TiO2: The Effect of Operational Parameters, Top. Catal, 63 (2020) 985-995.
[43] A.V. Karim, A. Shriwastav, Degradation of ciprofloxacin using photo, sono, and sonophotocatalytic oxidation with visible light and low-frequency ultrasound: Degradation kinetics and pathways, Chem. Eng. J, 392 (2020) 124853.
[44] M. Sarafraz, M. Sadeghi, A. Yazdanbakhsh, M.M. Amini, M. Sadani, A. Eslami, Enhanced photocatalytic degradation of ciprofloxacin by black Ti3+/N-TiO2 under visible LED light irradiation: Kinetic, energy consumption, degradation pathway, and toxicity assessment, Process Saf. Environ, 137 (2020) 261-272.
[45] R. Jothi Ramalingam, P. Arunachalam, T. Radhika, K.R. Anju, K.C. Nimitha, H.A. Al-Lohedan, Surface and electrochemical characterization of N-Fe-doped-TiO2 nanoparticle prepared by hydrothermal and facile electro-deposition method for visible light driven pollutant removal, Int. J. Electrochem. Sci, 12 (2017) 797-811.
[46] C.N.C. Hitam, A.A. Jalil, S. Triwahyono, A.F.A. Rahman, N.S. Hassan, N.F. Khusnun, S.F. Jamian, C.R. Mamat, W. Nabgan, A. Ahmad, Effect of carbon-interaction on structure-photoactivity of Cu doped amorphous TiO2 catalysts for visible-light-oriented oxidative desulphurization of dibenzothiophene, Fuel, 216 (2018) 407-417.
[47] M. Zarrabi, M.H. Entezari, E.K. Goharshadi, Photocatalytic oxidative desulfurization of dibenzothiophene by C/TiO2@MCM-41 nanoparticles under visible light and mild conditions, RSC Adv, 5 (2015) 34652-34662.
[48] E. Turiel, G. Bordin, A.R. Rodríguez, Study of the evolution and degradation products of ciprofloxacin and oxolinic acid in river water samples by HPLC-UV/MS/MS-MS, J. Environ. Monit, 7 (2005) 189-195.
[49] J. Cho, S. Jeon, S.A. Wilson, L.V. Liu, E.A. Kang, J.J. Braymer, M.H. Lim, B. Hedman, K.O. Hodgson, J.S. Valentine, E.I. Solomon, W. Nam, Structure and reactivity of a mononuclear non-haem iron(III)–peroxo complex, Nature, 478 (2011) 502-505.